Momentum-dependent relaxation dynamics of the doped repulsive Hubbard model

Sharareh Sayyad, Naoto Tsuji, Abolhassan Vaezi, Massimo Capone, Martin Eckstein, and Hideo Aoki

Phys. Rev. B **99**, 165132 — Published 22 April 2019

DOI: 10.1103/PhysRevB.99.165132

Momentum-dependent relaxation dynamics of the doped repulsive Hubbard model

Sharareh Sayyad,[1] Naoto Tsuji,[2] Abolhassan Vaezi,[3,4] Massimo Capone,[5,6] Martin Eckstein,[7] and Hideo Aoki[8,9]

[1]*Institute for Solid State Physics, University of Tokyo, Kashiwanoha, Kashiwa, Chiba 277-8581, Japan*
[2]*RIKEN Center for Emergent Matter Science (CEMS), Wako 351-0198, Japan*
[3]*Department of Physics, Stanford University, Stanford, CA 94305, USA*
[4]*Stanford Center for Topological Quantum Physics, Stanford University, Stanford, CA, USA*
[5]*International School for Advanced Studies (SISSA), Via Bonomea 265, I-34136 Trieste, Italy*
[6]*CNR-IOM Democritos, Via Bonomea 265, I-34136 Trieste, Italy*
[7]*Department of Physics, University of Erlangen-Nürnberg, 91058 Erlangen, Germany*
[8]*National Institute of Advanced Industrial Science and Technology (AIST), Tsukuba 305-8568, Japan*
[9]*Department of Physics, University of Tokyo, Tokyo 113-0033, Japan*

We study the dynamical behavior of doped electronic systems subject to a global ramp of the repulsive Hubbard interaction. We start with formulating a real-time generalization of the fluctuation-exchange approximation. Implementing this numerically, we investigate the weak-coupling regime of the Hubbard model both in the electron-doped and hole-doped regimes. The results show that both local and nonlocal (momentum-dependent) observables evolve toward a thermal state, although the temperature of the final state depends on the ramp duration and the band filling. We further reveal a momentum-dependent relaxation rate of the distribution function in doped systems, and trace back its physical origin to the anisotropic self-energies in the momentum space.

PACS numbers: 71.10.Hf, 71.30.+h, 71.27.+a, 74.72.Gh, 74.72.Ek

I. INTRODUCTION

There are increasing fascinations toward optimizing and controlling the properties of correlated systems in both experimental and theoretical studies. In particular, driving a system out of equilibrium by applying time-dependent modulations is a powerful avenue for realizing new quantum states. When the time-translational symmetry is broken in nonequilibrium situations , the initial thermal state can transform into a different state in a nonthermal fashion, since the time-dependent drive induces excitations of the correlated system. At short times, different non-thermal transients can emerge depending on the initial correlation and the preparation protocol. In the long-time limit, it is intriguing to see whether the system thermalizes or whether new correlations are built up that realize a long-lived nonthermal state. Achieving comprehensive insights requires, as discussed in the literature, incorporating details of the system that include the interplay of various degrees of freedom[1–5] lattice structures,[6,7] and doping concentrations[8].

In low-dimensional systems such as layered oxides or heterostructures, where strong nonlocal quantum correlation play a significant role, the doping level is a key control parameter, which leads to different regimes with different scattering mechanisms dominating.[9,10] This should leave fingerprints on the measured observables. In particular, the time-resolved optical conductivity after an excitation often shows a single or double exponential decay[11].

Measurements of Fermi-surface properties such as the momentum-dependent distribution function with the angle-resolved photoemission spectroscopy (ARPES) displays distinct temporal relaxation responses at different points on the Fermi surface.[4,5,12–14] Understanding the details of these is a formidable challenge due to the interplay between various degrees of freedom in a small energy range[10,15].

Nevertheless, it is imperative to understand the relaxation dynamics of doped systems, where the electron-electron interaction governs the physics. From a theoretical perspective, even when we focus on the simple one-band Hubbard model with an on-site repulsive interaction, investigation of the problem is quite challenging due to the nonequilibrium nature of the problem.

Incorporating spatially nonlocal correlations in two dimensions is computationally demanding as in nonequilibrium dynamical cluster approximation (DCA)[16], diagrammatic approaches[17,18], and variational Monte Carlo method[19], while the well-developed one-dimensional[20,21] and infinite-dimensional[22] nonequilibrium algorithms cannot directly treat two-dimensional systems. A large number of investigations have been devoted to understanding the long-time dynamics of fermionic systems, at half filling, after a global ramp of the interaction parameter.[16,17,23–25] In these attempts, the long-time thermalization occurs for nearly all the weak electron-electron coupling regimes, which sometimes supersedes intermediate pre-thermalization plateaus.[17,23,25] Away from the half-filling, on the other hand, investigations of doped systems in infinite dimensions reveal that the observed sharp dynamical transition from an exponential relaxation in the weak-coupling regime to an oscillating behavior in the strong-coupling regime is smoothened into a crossover between these two regimes.[25] In two dimensions, studies for half-filled systems reveal a *momentum-dependent relaxation* of the single-particle momentum distribution after a sudden quench of the electron-electron interaction.[16,17] However, we are still left with important questions as to (i) how these dynamical behaviors vary in doped systems, (ii) what would be the effect of finite ramp durations (as opposed to sudden quenches), and (iii) to what extent the relaxation dynamics depends on the momentum in the Brillouin zone.

In the present work we precisely address these questions in both the electron-doped and hole-doped systems. We employ an interaction ramp protocol on a two-dimensional system

with repulsive electron-electron interaction. We formulate the real-time generalization of the fluctuation-exchange approximation (FLEX)[26–29]. It is known that this algorithm, with vertex corrections ignored, cannot address the intermediate and strong-coupling regimes where the Mott insulator starts to emerge.[30] Also, underdoped systems exhibit, at low temperatures, pseudogap physics which requires an extension of the FLEX.[31] We thus limit ourselves to the weak-coupling regime and at temperatures where pseudogap does not emerge. We shall show that there exist a rapid local thermalization of the system, where the ramp duration determines the temperature. More importantly, using the nonequilibrium FLEX, we can analyze the *momentum-dependent evolution* of both single- and two-particle observables. Namely, we shall show that there exists a doping-dependent nodal-antinodal dichotomy in the relaxation rate of the single-particle momentum distributions.

This paper is organized as follows. We define the model Hamiltonian and present the proposed numerical algorithm in Sec. II. In Sec. III we present numerical results and discuss the underlying physics. Section IV is devoted to conclusions of this work.

II. MODEL AND METHOD

A. Model Hamiltonian

The repulsive one-band Hubbard model on the square lattice is defined as

$$H = -\sum_{ij,\sigma}\left(v_{|i-j|}c^\dagger_{i\sigma}c_{j\sigma} + \text{h.c.}\right) + \sum_i U(t)\left(n_{i\uparrow}-\frac{1}{2}\right)\left(n_{i\downarrow}-\frac{1}{2}\right) - \mu\sum_{i,\sigma} n_{i\sigma}, \quad (1)$$

where $c^\dagger_{i\sigma}$ creates an electron with spin σ at site i, $n_{i\sigma} = c^\dagger_{i\sigma}c_{i\sigma}$, and opposite spins experience a local repulsive interaction U, which is here assumed to be time-dependent. The band filling is set by the chemical potential μ. $v_{|i-j|}$ stands for the hopping amplitude from site i to a neighboring site j, which is taken here up to the third-neighbors. We then have a band dispersion on the square lattice as

$$\varepsilon_{\boldsymbol{k}} = -2v_1\big[\cos(k_x)+\cos(k_y)\big] - 4v_2\cos(k_x)\cos(k_y) - 2v_3\big[\cos(2k_x)+\cos(2k_y)\big], \quad (2)$$

where $\boldsymbol{k} = (k_x, k_y)$ is the two-dimensional momentum, and hopping parameters are here set to $v_2 = -0.2v_1$, and $v_3 = 0.16v_1$, relevant for the the copper-oxygen planes of high-temperature superconductors[32,33], see solid green line in Fig. 7 (lower panel). We report our results in the energy (time) unit of v_1 ($1/v_1$).

To explore the thermalization of doped quantum systems, we take the Hubbard model where the Hubbard interaction is switched on with a ramp (see Fig.1),

$$U(t) = \begin{cases} U_{\rm f}\left[1-\cos(\frac{\pi t}{2t_{\rm r}})\right] & \text{for} \quad t \le t_{\rm r}, \\ U_{\rm f} & \text{for} \quad t > t_{\rm r}, \end{cases} \quad (3)$$

with $t_{\rm r}$ the ramp duration, and $U_{\rm f}$ the final Hubbard interaction. This protocol can directly be realized in cold-atom setups[34], or can indirectly be realized in solids excited by a short few-cycle laser pulse[35] in terms of the effective electron-electron interaction. The FLEX is reliable in the weak-coupling regime, so that we set the final Hubbard interaction to $U_{\rm f} \le 3$ for which $U_{\rm f}$ is much smaller than the band width ($= 7.7$ for the present choice of the hopping parameters). The initial temperature $T = 1/\beta = 1/20$ is chosen so that the system is away from superconducting and antiferromagnetic phases.

B. Numerical method

We perform the numerical investigations of our model in finite-temeprature paramagnetic phases where no long-range order is present, and use, for nonequilibrium situations, the Schwinger-Keldysh[36,37] generalization of the FLEX[26–28]. Incorporated Feynman graphs in this diagrammatic formalism are determined from a functional derivative of the Luttinger-Ward functional,[38] and thus the approach is a conserving approximation.[26,39] It has been well established that in the weak-coupling regime the results are qualitatively in good agreement with numerically exact quantum Monte-Carlo results.[40] One technical detail is that the self-energy diagrams have been collected here with an assumption that the expectation value of the pair correlation is negligible and thus the anomalous contributions can be omitted. This particular choice implies that our formalism is applicable to studying normal phases as well as the behavior of the system just at an instability to superconductivity.

In the FLEX, the electron scattering incorporates the magnetic, density, and also singlet-pairing channels. Correspondingly, we consider the spin susceptibility (χ^s), charge susceptibility (χ^c), and, here in particular, the particle-particle susceptibility (χ^{pp}). The latter is important, since it enables us to examine the effects of pair fluctuations represented by the particle-particle susceptibility, defined in terms of the pair operator, $\Delta_{\boldsymbol{k}}(t) \equiv c_{\boldsymbol{k}\uparrow}(t)c_{-\boldsymbol{k}\downarrow}(t)$, as

$$\chi^{pp}_{\boldsymbol{k}}(t,t') = -i\langle \mathcal{T}_{\mathcal{C}}\Delta_{\boldsymbol{k}}(t)\Delta^\dagger_{-\boldsymbol{k}}(t')\rangle, \quad (4)$$

where $\mathcal{T}_{\mathcal{C}}$ is the time-ordering operator on the Keldysh contour $\mathcal{C}$.

The spin, charge, and particle-particle susceptibilities obey algebraic equations which are obtained in FLEX by summing geometric series of ladder and bubble diagrams as

$$\chi^r_{\boldsymbol{q}}(t,t') = U(t)\chi^{0r}_{\boldsymbol{q}}(t,t')U(t') + s_r\big[\chi^{0r}_{\boldsymbol{q}} * U * \chi^r_{\boldsymbol{q}}\big](t,t'), \quad (5)$$

where $r \in \{s, c, pp\}$ denotes the channel with s_r has $s_s = s_{pp} = -1, s_c = 1$. The crystal momentum $\boldsymbol{q}$ resides, in

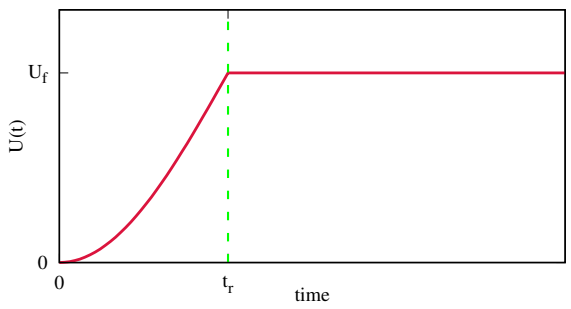

Figure 1. Ramp up of the Hubbard interaction given in Eq. (3).

numerical calculations, on a $N_k \times N_k$ momentum grid with $\sum_{\boldsymbol{q}} = N_k^2$. In nonequilibrium situations, every susceptibility has two time arguments due to the broken time-translational invariance, so we require two time arguments t, t', defined on the Schwinger-Keldysh contour $\mathcal{C}$, and "$*$" stands for the convolution integral on $\mathcal{C}$. χ^{0r} is the polarization function computed by

$$\chi^{0c/s}_{\boldsymbol{q}\sigma\sigma'}(t,t') = \frac{i}{N_k^2}\sum_{\boldsymbol{k}} G_{\boldsymbol{k}+\boldsymbol{q}\sigma}(t,t')G_{\boldsymbol{k}\sigma'}(t',t), \tag{6}$$

$$\chi^{0pp}_{\boldsymbol{q},\sigma\overline{\sigma}}(t,t') = \frac{i}{N_k^2}\sum_{\boldsymbol{k}} G_{\boldsymbol{k}+\boldsymbol{q}\sigma}(t,t')G_{-\boldsymbol{k}\overline{\sigma}}(t,t'), \tag{7}$$

where $\overline{\sigma} \equiv -\sigma$, and G is the interacting Green's function,

$$G_{\boldsymbol{k}\sigma}(t,t') = -i\langle \mathcal{T}_{\mathcal{C}}[c_{\boldsymbol{k}\sigma}(t)c^{\dagger}_{\boldsymbol{k}\sigma}(t')]\rangle. \tag{8}$$

We note that in the paramagnetic phase we have $G_{\boldsymbol{k}\sigma} = G_{\boldsymbol{k}-\sigma}$. The employed diagrammatic expansions for computing four-point correlation functions in Eq. 5 comprise all the topologies of diagrams up to the third-order interaction expansions, while for higher orders they ignore a large number of diagrams that include vertex corrections[41], such that the remained set of diagrams is reducible in the particle-particle or particle-hole channels.

An important consequence of this choice arises in the generic two-particle correlation function,

$$\mathcal{O}^{\sigma_1\sigma_2\sigma_3\sigma_4}_{\boldsymbol{k}_1\boldsymbol{k}_2\boldsymbol{k}_3\boldsymbol{k}_1+\boldsymbol{k}_2-\boldsymbol{k}_3}(t_1,t_2,t_3,t_4) = -i\langle o_{\sigma_1\boldsymbol{k}_1}(t_1)o_{\sigma_2\boldsymbol{k}_2}(t_2)o^{\dagger}_{\sigma_3\boldsymbol{k}_3}(t_3)o^{\dagger}_{\sigma_4\boldsymbol{k}_1+\boldsymbol{k}_2-\boldsymbol{k}_3}(t_4)\rangle, \tag{9}$$

where $o_{\sigma_i\boldsymbol{k}}(o^{\dagger}_{\sigma_i\boldsymbol{k}})$ is a one-particle annihilation (creation) operator with spin σ_i and momentum $\boldsymbol{k}$. There, the present choice reduces, in the presence of the energy and momentum conservation, the number of independent momenta to two cases, where $(\boldsymbol{k}_1,\boldsymbol{k}_2,\boldsymbol{k}_3) \in \{(\boldsymbol{k},\boldsymbol{k}+\boldsymbol{q},\boldsymbol{k}),(-\boldsymbol{k},\boldsymbol{k}+\boldsymbol{q},-\boldsymbol{k})\}$, associated with bubble and ladder diagrams, see Eqs. 6 and 7. The independent time indices are reduced to two as $(t_1,t_2,t_3,t_4) = (t,t',t,t')$. In the paramagnetic phase, only two different spin combinations arise as $(\sigma_1\sigma_2\sigma_3\sigma_4) \in \{(\sigma,\sigma,\sigma,\sigma),(\sigma,\overline{\sigma},\overline{\sigma},\sigma)\}$.

Equal spins which occur in the particle-hole channel contribute to the charge and the transverse (z-component) spin

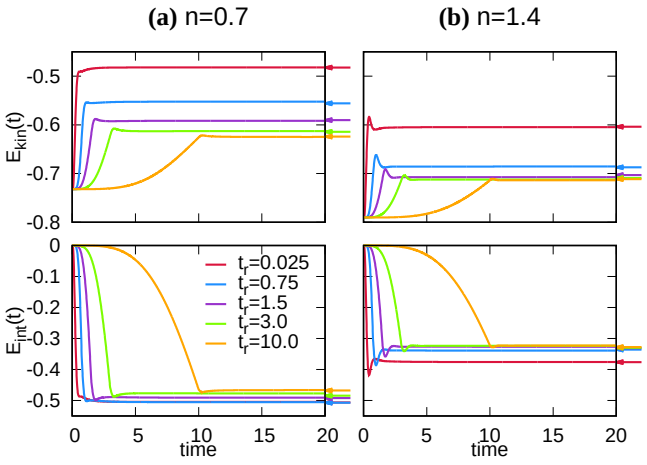

Figure 2. Kinetic energy (top panels) and interaction energy (bottom) as a function of time for various ramp durations $t_{\rm r} = 0.025 - 10.0$ at fillings n =0.7 (a) or 1.4 (b). Arrows indicate the expected thermal values at $t = 20$ for each value of $t_{\rm r}$.

fluctuations. Two other components of the spin susceptibilities, i.e., the longitudinal (x and y) components, as well as the reduced four-point correlation function in the particle-particle channel, have a relevant spin configuration of the form $(\sigma,\overline{\sigma},\overline{\sigma},\sigma)$. In the paramagnetic phase, the three components of the spin susceptibility should be equal, resulting in a factor of 3 in Eq. 13. Hence, for brevity purpose, we omit the spin indices in Eq. 6. Besides, the electron-electron interaction is instantaneous in time and local in space (for the on-site Hubbard model), which imposes that at each vertex of the two-body operator in the bubble and ladder diagrams, the time arguments and site indices should be, respectively, the same. As a result, only two time arguments remain independent, and we should sum over one of the two momenta, which leaves us only two different site indices for four-point correlation functions.

The single-particle propagator satisfies the Dyson equation,

$$\begin{aligned}&\left(i\partial_t + \mu - \Sigma^{\rm H}_{\sigma} - \varepsilon_{\boldsymbol{k}}\right)\mathcal{G}_{\boldsymbol{k}\sigma}(t,t') = \delta_{\mathcal{C}}(t,t'),\\ &G_{\boldsymbol{k}\sigma}(t,t') = \mathcal{G}_{\boldsymbol{k}\sigma}(t,t') + \left[\mathcal{G}_{\boldsymbol{k}\sigma} * \Sigma^{\rm FLEX}_{\boldsymbol{k}\sigma} * G_{\boldsymbol{k}\sigma}\right](t,t'),\end{aligned} \tag{10}$$

where $\mathcal{G}$ is the noninteracting Green's function. The local density of electrons is given as

$$n_{\sigma}(t) = \frac{1}{N_k^2}\sum_{\boldsymbol{k}} {\rm Im}[G^{<}_{\boldsymbol{k}\sigma}](t,t),$$

where $G^{<}$ is the lesser component of the Green's function with $t < t'$ in Eq. 8. The Hartree self-energy is then given by

$$\Sigma^{\rm H}_{\sigma}(t) = \frac{1}{2}U(t)n_{\sigma}(t). \tag{11}$$

Within FLEX the electronic self-energy is given as

$$\begin{aligned}\Sigma^{\rm FLEX}_{\boldsymbol{k}\sigma}(t,t') = &-\frac{i}{N_k^2}\sum_{\boldsymbol{q}} \Gamma^{ph}_{\boldsymbol{q}}(t,t')G_{\boldsymbol{k}-\boldsymbol{q}\sigma}(t,t')\\ &-\frac{i}{N_k^2}\sum_{\boldsymbol{q}} \Gamma^{pp}_{\boldsymbol{q}}(t,t')G_{\boldsymbol{q}-\boldsymbol{k}\overline{\sigma}}(t',t),\end{aligned} \tag{12}$$

where $\overline{\sigma} = -\sigma$, the particle-hole ($ph$) and particle-particle (pp) vertex functions are evaluated by sums of bubble and ladder diagrams as

$$\Gamma^{ph}_{\boldsymbol{q}}(t,t') = \frac{1}{2}\chi^{c}_{\boldsymbol{q}}(t,t') + \frac{3}{2}\chi^{s}_{\boldsymbol{q}}(t,t') - U(t)\chi^{0s}_{\boldsymbol{q}}(t,t')U(t'),$$
$$\Gamma^{pp}_{\boldsymbol{q}}(t,t') = \chi^{pp}_{\boldsymbol{q}}(t,t') + U(t)\chi^{0pp}_{\boldsymbol{q}}(t,t')U(t'). \quad (13)$$

In the following, we report our results computed on a lattice with 64×64 momentum-space discretization. Due to memory limitation for saving two-time Green's functions, we cease simulating the system after $t_{\max} = 20$.

C. Observables

Observables which we are interested in the nonequilibrium dynamics are:

a. Kinetic energy of the system, which is calculated as

$$E_{\rm kin} = \frac{1}{N_k^2}\sum_{\boldsymbol{k}\sigma} \mathrm{Im}\big[\varepsilon_{\boldsymbol{k}\sigma} G^{<}_{\boldsymbol{k}\sigma}\big](t,t). \quad (14)$$

b. Interaction energy, which is evaluated as

$$E_{\rm int} = \frac{1}{N_k^2}\sum_{\boldsymbol{k}\sigma} \mathrm{Im}\big[\Sigma^{\rm FLEX}_{\boldsymbol{k}\sigma} * G_{\boldsymbol{k}\sigma}\big]^{<}(t,t), \quad (15)$$

where "$*$" again denotes the convolution.

c. Total energy, which is

$$E_{\rm tot} = E_{\rm kin} + E_{\rm int}. \quad (16)$$

The effective temperature of relaxed systems is defined as the equilibrium thermal state whose total energy is the same as the driven system at a given time.

d. Momentum-dependent distribution function, which is given by

$$n_{\boldsymbol{k}} = -\frac{1}{2}\sum_{\sigma} \mathrm{Im}\big[G_{\boldsymbol{k}\sigma}\big]^{<}(t,t). \quad (17)$$

e. Jump of the distribution function. The jump of the momentum-dependent distribution function is evaluated as

$$\Delta n_{\boldsymbol{k}_{\rm f}} = n_{\boldsymbol{k}_{\rm f}-\boldsymbol{\delta}} - n_{\boldsymbol{k}_{\rm f}+\boldsymbol{\delta}}, \quad (18)$$

where the non-interacting Fermi momenta $\{\boldsymbol{k}_{\rm f}\}$ satisfy $\varepsilon_{\boldsymbol{k}_{\rm f}} - \mu = 0$. As our system is initially prepared in the non-interacting regime ($U(t = 0) = 0$), this choice of the Fermi momenta corresponds to the Fermi sea as the initial state. Because we are exploring momentum-dependent relaxations, we pay particular attention to this quantity at two directions in the Brilloun zone; along the "nodal direction" $\Gamma(0,0) - M(\pi,\pi)$ with $\boldsymbol{\delta}$ along (1,1) direction with N_k discretized points over 2π. As for the "antinodal region" we can look at the $X(\pi,0) - M(\pi,\pi)$ direction [with $\boldsymbol{\delta}$ along (0,1)] which the Fermi surface intersects (while Γ - X does not for the hole-doped case).

f. Photo-emission spectrum (PES), which can be probed by a Gaussian pulse $S(t) = \exp(-t^2/2\alpha^2)$ with the time resolution $\alpha(= 3$ here to smear the Fourier artifacts for short-time simulations), is given by the spectral function,[42]

$$A^{<}_{\boldsymbol{k}}(\omega,t) \equiv \quad (19)$$
$$-\frac{\mathrm{i}}{4\pi}\sum_{\sigma}\int \mathrm{d}t_1\mathrm{d}t_2 S(t_1)S(t_2)e^{\mathrm{i}\omega(t_1-t_2)}G^{<}_{\boldsymbol{k}\sigma}(t+t_1,t+t_2).$$

To minimize the overlaps between the initial ramp protocol and PES, we only use the probe pulse inside the window of $[-2\alpha, 2\alpha]$ and consequently the time arguments in Eq. 19 run in this range.

To present a time-dependent momentum-resolved PES $A_{\boldsymbol{k}}(\omega,t)$, we substitute the lesser Green's function with the retarded Green's function ($G^{\rm ret}_{\boldsymbol{k}}$). Calculating the density of state $A_{\rm loc}(\omega,t)$ is then very straightforward as we employ the local retarded Green's function,

$$G^{\rm ret}_{{\rm loc}\sigma}(t,t') = \frac{1}{N_k^2}\sum_{\boldsymbol{k}} G^{\rm ret}_{\boldsymbol{k}\sigma}(t,t'), \quad (20)$$

instead of the $G^{<}_{\boldsymbol{k}\sigma}$ in Eq. 19. The obtained spectrum A is broader than the physical spectral function as it is convoluted with the Gaussian function. One should note that, although evaluating the spectral function is straightforward, obtaining a high-resolution spectrum out of our short-time simulations is accompanied by Fourier artifacts. We thus smear these artifacts by convoluting the real-time Green's function with a fairly broad Gaussian filter.

The renormalized dispersion relation ($\widetilde{\varepsilon}_{\boldsymbol{k}}$) at time t is obtained from the position of the quasiparticle peak ($\omega_{\rm qp}$) in $A_{\boldsymbol{k}}(\omega_{\rm qp},t) - U(t)n(t)/2$, where the factor $U(t)n(t)/2$ is the Hartree term, see Eq. 10.

g. Interacting and noninteracting Fermi surfaces. The bare (noninteracting) Fermi momenta at $U(t = 0) = 0$ are obtained by solving $\varepsilon_{\boldsymbol{k}} - \mu = 0$. In the presence of electron-electron interaction ($U(t) > 0$) momenta on the Fermi surface are defined by $\widetilde{\varepsilon}_{\boldsymbol{k}} - \mu = 0$.

h. Spin, charge, and particle-particle correlation functions. The equal-time spin (s), charge (c), and particle-particle (pp) correlation functions are given by

$$\chi^{r}_{k}(t) = |\mathrm{Im}\left[\chi^{r<}_{k}(t,t)\right]|, \quad (21)$$

where $\chi^{r<}_{k}$ denotes the lesser component of the Keldysh susceptibility with the channel index $r \in \{s, c, pp\}$.

III. RESULTS AND DISCUSSIONS

A. Local observables

Let us first look at the kinetic and potential energies of the hole-doped ($n = 0.7$) and electron-doped ($n = 1.4$) systems under various ramp durations, $t_{\rm r}$ = 0.025, 0.75, 1.5, 3.0 and 10.0, in Fig. 2. Note here that the nonzero next-neighbor hopping in Eq. 1 breaks the particle-hole symmetry. Thus, instead of n and $2 - n$, we prefer to study hole- and electron-doped

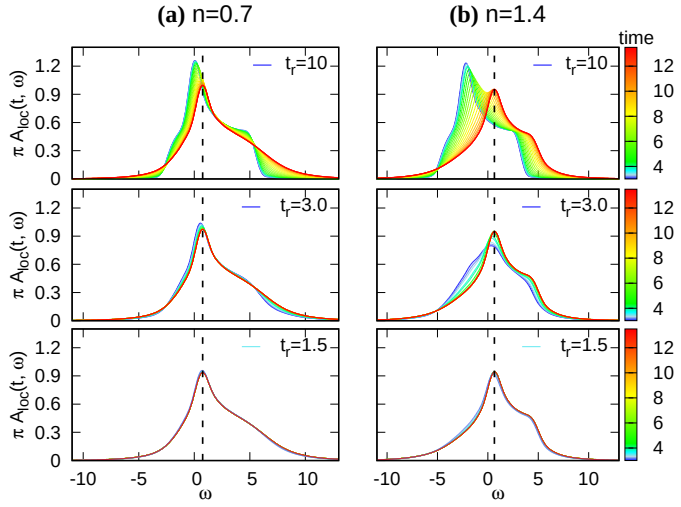

Figure 3. The PES for ramp durations $t_{\rm r} = 1.5$, 3.0, and 10.0 for $U_{\rm f} = 3$, $\beta = 20$. Vertically aligned panels belong to the same fillings, namely $n = 0.7$ (a), and 1.4 (b). The color coding refers to time. Vertical dashed lines indicate the respective position of the quasiparticle peak at $\omega = 0.75$ for $n = 0.7$ and $\omega = 0.65$ for $n = 1.4$ after the final stage of ramping ($t > t_{\rm r}$).

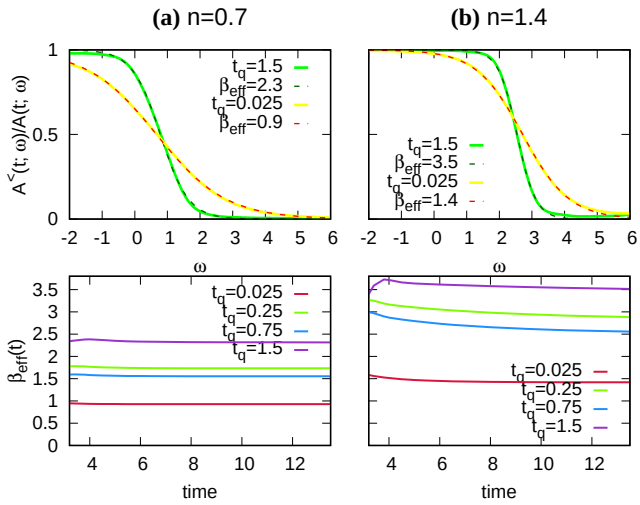

Figure 4. For hole-doped ($n = 0.7$) (a) and electron-doped ($n = 1.4$) (b) regimes, the upper panels plot the ratio $A^<(t,\omega)/A(t,\omega)$ at $t = 13.5$ for ramp durations $t_{\rm r} = 0.025$ (yellow solid lines) and 1.5 (cyan solid lines). Dashed lines are fits with the Fermi distribution with the indicated effective inverse temperature, $\beta_{\rm eff}$. Lower panels plot the $\beta_{\rm eff}$ against time for $t_{\rm r} = 0.025$ (red), 0.25 (green), 0.75 (blue), and 1.5 (purple), again for the hole-doped (left panel) and electron-doped (right) cases.

cases with the chemical potential $\mu_h = -\mu_e$, which respectively corresponds to $n = 0.7$ and $n = 1.4$, where the systems are in the over-doped regimes with the pseudogap absebt, and we are sufficiently far from the Mott insulator. Switching on of the Hubbard interaction naturally has a vast effect on the interaction energy for $t < t_{\rm r}$ as seen in lower panels of Fig. 2. The kinetic energy also exhibits a large transient response for $t < t_{\rm r}$, see upper panels of Figs. 2. We can see that the overall change in the kinetic energy strongly depends on whether we sit on the hole-doped or electron-doped side. This is not unexpected for two reasons: (i) our system has the particle-hole asymmetry with different densities of states at the Fermi energy between hole-doped and electron-doped regimes, and (ii) an obvious effect in an electron-doped system of smaller numbers of empty sites aside from the thermally generated holons (and doublons), which forces the electrons to hop to doubly-occupied sites. In the hole-doped case, hopping to empty sites is easier, and we have a stronger change in the kinetic energy, see upper panel of Fig. 2(a).

For $t > t_r$, a kink in the ramp functional form in Eq. 3 results in the appearance of a bump in short-time evolutions of both the kinetic and interaction energies, which are more pronounced in the electron-doped regime due to the excess number of doubly occupied sites. For longer ramp durations the system has a long time to redistribute its electronic configuration during $t < t_r$ so that the transient bump is less evident.

To further corroborate local thermalization of the system, we present the time-evolution of the PES spectrum of systems under various ramp durations, $t_{\rm r} = 0.75$, 1.5, and 10.0, in the hole-doped ($n = 0.7$) and electron-doped ($n = 1.4$) regimes in Fig. 3. For short ramps, the result confirms a rapid relaxation of spectrum in all doping regimes, as time-dependent spectrum, plotted with different colors, are hardly distinguishable for $t > 6$. For a long ramp ($t_{\rm r} = 10$), the evolution of PES is considerable during the preparation period ($t_{\rm r}$), and the evolution quickly terminates shortly after $t_{\rm r}$. We can also note that, at long times when the probe envelope, centered around $t > t_{\rm r}$, overlaps with the initial ramp protocol, the evolution of PES is not an intrinsic relaxation. At the time at which local observables become stationary, i.e., $t = 13.5$ here, the spectral density also becomes time-independent, where the position of the quasiparticle peak, independent of the ramp duration, exhibits doping-dependent values as $\omega = 0.75$ for $n = 0.7$ and $\omega = 0.65$ for $n = 1.4$, see dashed lines in Fig. 3.

We can further assess the thermal nature of the spectrum by looking at the ratio $A^<(t,\omega)/A(t,\omega)$ in the upper panels of Figs. 4, since the fluctuation-dissipation theorem dictates that this ratio should be, in a thermal state, equal to the Fermi-Dirac distribution function as

$$\frac{A^<(t,\omega)}{A(t,\omega)} = \frac{1}{1+\exp\left[\beta_{\rm eff}(t)\big(\omega-\mu_{\rm eff}\big)\right]}. \qquad (22)$$

By fitting the spectrum with Eq. (22), we evaluate the inverse, $\beta_{\rm eff}(t)$, of the time-dependent effective temperature. Consistent with the adiabatic theorem, doped systems with longer ramp durations are effectively colder, see lower panels of Fig. 4. Comparing the effective temperatures of the system with the same preparation protocol shows that hole-doped systems become hotter than electron-doped systems. To be precise, the effective temperatures in Fig. 4, derived from a Gaussian-broadened spectrum, are slightly over-estimated, but the trend should be robust. This analysis remains valid irrespective of whether the Fermi-liquid picture is present or violated.

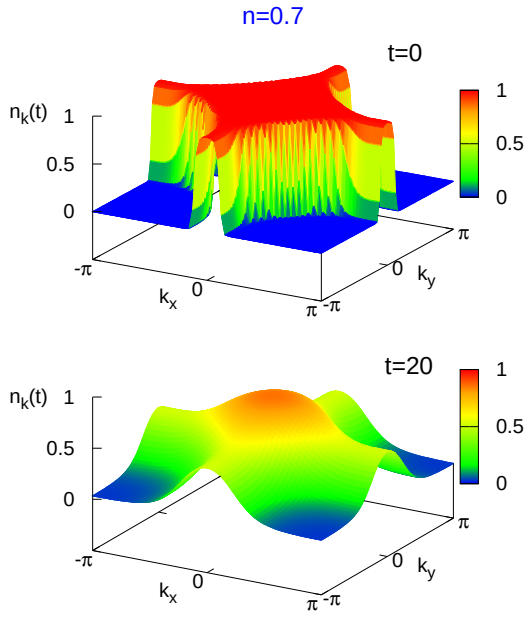

Figure 5. For a hole-doped filling $n = 0.7$ the momentum-dependent distribution function at initial ($t = 0$; top panel) and final ($t = 20$; bottom) times are plotted for $U_f = 3$ and $\beta = 30$ and $t_r = 0.25$.

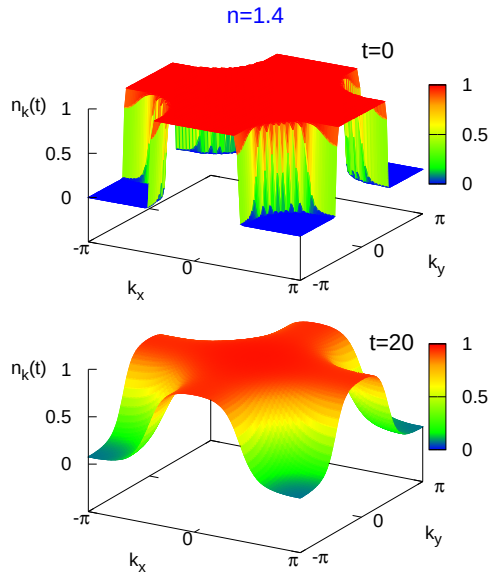

Figure 6. For an electron-doped filling $n = 1.4$ the momentum-dependent distribution function at initial ($t = 0$; top panel) and final ($t = 20$; bottom) times for $U_f = 3$ and $\beta = 30$ and $t_r = 0.25$.

B. Momentum-dependent observables

Let us now move on to the momentum-dependent distribution functions at initial and final times in a hole-doped ($n = 0.7$) system in Fig. 5, and an electron-doped ($n = 1.4$) system in Fig.6, with $t_r = 0.25$. A sharp jump of n_k at the Fermi wavenumber at initial times, associated with the Fermi-Dirac distribution at $\beta = 20$, is significantly smeared at $t = 20$ in both systems. This is consistent with a general intuition that occupation of excited states will elevate the effective temperature after pumping.

If we now turn to the upper panels of Fig. 7, which plots momentum-resolved PES of both hole-doped ($n = 0.7$) (a) and electron-doped ($n = 1.4$) (b) regimes, we can see that the widths of the momentum-dependent spectrum at the Fermi momenta (red along XM and green ΓM in the top panels) are wider for the hole-doped case, which indicates more heating than in the electron-doped system. We further observe a doping-dependent evolution in $n_{\boldsymbol{k}}$, where the redistribution of occupation in the hole-doped system is so drastic that the occupied region even deforms from an open Fermi sea into a closed one, which may be called a "nonequilibrium Lifshitz transition", see Fig. 5. We can then look at the renormalized dispersion relations in Fig. 7 (c) for the hole-doped ($n = 0.7$) and electron-doped ($n = 1.4$) systems, extracted from the spectra displayed in upper panels of Fig. 7. The band renormalization is not dramatic as we expect for the weak-coupling physics. The deformation of the Fermi surface in the electron-doped regime (dashed blue arrows at $t = 0$ and solid blue arrows at $t = 13.5$) is less considerable than in the hole-doped regime (dashed red arrows at $t = 0$ and solid red arrows at $t = 13.5$). This endorses the nonequilibrium Lifshitz transition for $n_{\boldsymbol{k}}$ in Fig. 5.

To further characterize the dynamical behavior of $n_{\boldsymbol{k}}$ and its doping dependence, Fig. 8 plots the jump, $\Delta n_{\boldsymbol{k}}$, of the momentum-dependent occupation around the bare noninteracting Fermi energy at two Fermi momenta along ΓM and XM directions, respectively, in hole-doped and electron-doped regimes, where the Fermi momenta refer to the initial noninteracting Fermi surface for $U(t = 0) = 0$.

After t_r, a transient correlation built-up timescale $\sim 1/v_1$ is observed, see vertical lines in Fig. 8.[17,43] This short-time response is followed by an exponential relaxation dynamics in all the cases. The initial preparation protocol and the doping concentrations govern these momentum-dependent evolutions: For the longer ramp durations, the system finds the opportunity to adjust the injected energy and occupies less excited states. Namely, the system effectively experiences less heating and consequently the correlation-based relaxation, in contrast to thermal relaxation for small t_r, rules the dynamics for long ramps. This over-heating picture is indeed consistent with extensively discussed half-filled results for infinite dimensional[23,25,43,44] and two-dimensional[16,17] systems.

A salient feature is that the relaxation dynamics is distinct, in agreement with Fig. 8, between the Fermi momenta along the XM and along the ΓM directions, as previously found with nonequilibrium DCA.[16] To quantify this behavior of Δn_k at finite dopings, we fit our results to an exponential function of the form $f(t) \sim c_0 + c_1 \exp(-t/\tau)$, where c_0 and c_1 are constants, and τ is the relaxation time. Figure 9 summarizes the result for $1/\tau$ against the band filling along the XM and ΓM directions, respectively, for various values of the ramp duration, t_r (color-coded). We can see that τ significantly depends on the three factors: doping, the position of the Fermi momentum and the ramp duration. Namely, the result first shows that the scattering rate ($1/\tau$) decreases

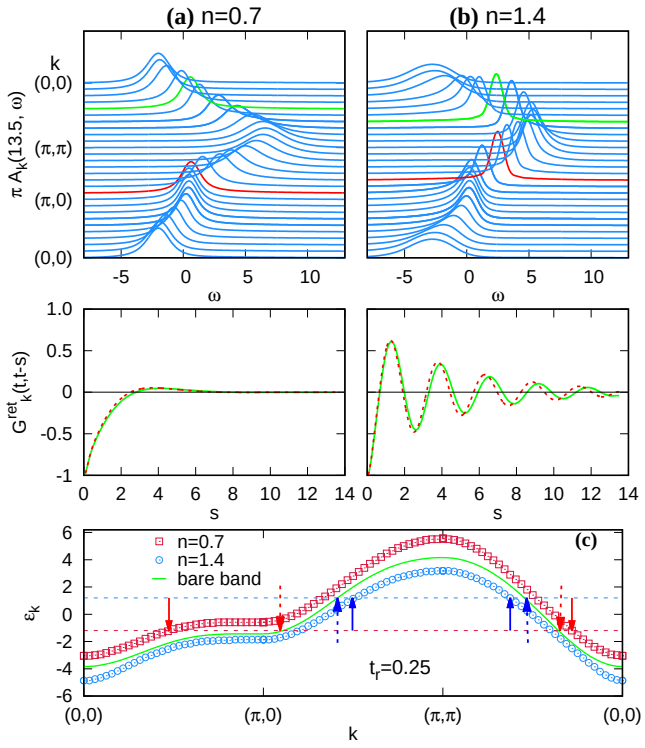

Figure 7. Top panels: The PES $A_{\boldsymbol{k}}(t,\omega)$ at $t = 13.5$ in the hole-doped ($n = 0.7$) (a) and electron-doped ($n = 1.4$) (b) regimes for $t_{\rm r} = 0.25$. The vertical axis is the momentum, with small offsets for the spectra for clarity. Red (green) line represents the PES at initial Fermi momenta along XM (ΓM). Middle panels: The retarded Green's functions $G^{\rm ret}_{\boldsymbol{k}}(t,t-s)$ at $t = 13.5$ for hole-doped ($n = 0.7$; left panel) and electron-doped ($n = 1.4$; right) cases. Color lines correspond to the spectra with the same colors in upper panels, respectively. (c) The dispersion relation for the noninteracting inital band given in Eq. (2) (solid green line), the renormalized band for the hole-doped ($n = 0.7$) (red open squares) and for the electron-doped ($n = 1.4$) (blue open circles) systems. Dashed (solid) arrows attached to each dispersion relation indicate the Fermi momenta at $t = 0$ ($t = 13.5$). Horizontal dashed lines represent the chemical potentials for the hole-doped ($n = 0.7$) (red) and the electron-doped ($n = 1.4$) (blue) systems.

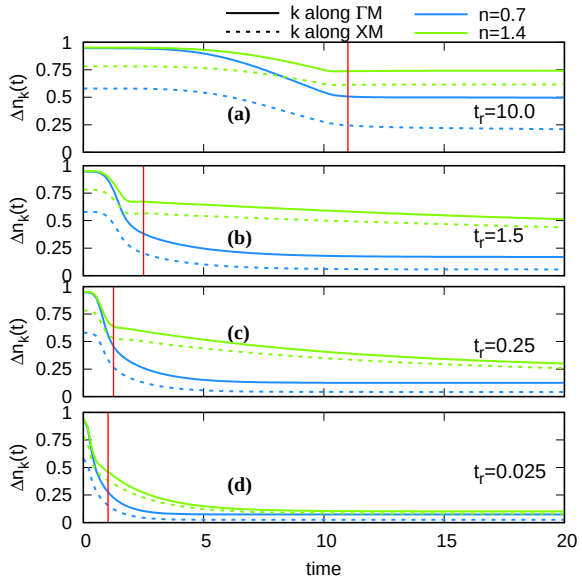

Figure 8. The jump, $\Delta n_{\boldsymbol{k}}$, of the momentum-dependent distribution function for ramp durations $t_{\rm r} = 10$ (a), 1.5 (b), 0.25 (c), and 0.025 (d) at initial Fermi momenta along ΓM (solid line) or XM (dashed line) for the hole-doped ($n = 0.7$) (blue) and electron-doped ($n = 1.4$) (green) systems. A vertical red line indicates the transient built-up duration, $t_{\rm r} + 1/J_1$, for each panel.

with the increased density of electrons from hole-doped to electron-doped regimes. Secondly, consistent with the previous undoped DCA result,[16] the relaxation time is smaller at the hot spot along XM. These two features hint at an effect of a momentum-dependent self-energy in the correlated system. Thirdly, for long preparation protocols where heating is mitigated, the non-thermal state has longer lifetimes.

We can also see in Fig. 10(a) that a stronger electron-electron interaction enhances the scattering rate $1/\tau$ and thus expedite the relaxation. We also note that the undoped results relaxed at higher temperatures, where Mott insulating phase does not find a room to emerge, and consequently the results are reliable.

We have found that the width of the quasiparticle peaks around the Fermi surface is generically smaller in the electron-doped systems than in the hole-doped ones. This width is, in the thermal states in the Fermi liquid theory, proportional to the imaginary part of the retarded self-energy, so that the result implies smaller incoherent contributions to the scattering rate in the electron-doped systems. This observation then suggests that thermal relaxations are more dominant in the hole-doped systems where the effective local temperature is larger.

To reinforce this argument, let us directly look at $\Sigma^{\rm ret}_{\boldsymbol{k}}(t,\omega_{\rm qp})$ both in the hole-doped ($n = 0.7$) and electron-doped ($n = 1.4$) regimes, where $\omega_{\rm qp}$ denotes the quasiparticle energy, which is determined from a near Lorentzian spectrum presented in upper panels of Fig. 7. As we can see from red and green lines there, $\omega_{\rm qp} = 0.55$ for the hole-doped case ($n = 0.7$), and $\omega_{\rm qp} = 2.35$ for the electron-doped one ($n = 1.4$) for $t_{\rm r} = 0.25$. In Fig. 9, lower panels plot $|{\rm Im}\Sigma^{\rm ret}_{\boldsymbol{k}}(t,\omega_{\rm qp})|$ at $t = 13.5$ at which the local relaxation for $t_{\rm r} = 0.25$ is almost attained. We have also checked that for $t_{\rm r} = 10$, the $\omega_{\rm qp}$ is slightly smaller than that for $t_{\rm r} = 0.25$.

In the anisotropic self-energies for the quasiparticle with the energy $\omega_{\rm qp}$ in Fig.9, where squares (circles) mark the Fermi points along ΓM (XM), the hole-doped case exposes elevated interacting regions preferentially around X point ($(\pi,0)$) in the Brillouin zone. In the electron-doped case, the elevated interacting regions lie along the Fermi surface. Moreover, in colder systems for larger $t_{\rm r}$, the overall value of the self-energy is smaller, which implies that the quasiparticle has a longer lifetime, in agreement with a slower decay rate of Δn_k for longer ramps, see Fig. 8. This behavior is also evident in the temporal evolution of the two-time retarded Green's function, see middle panels of Fig. 7, where the associated electron-doped Green's function exhibits a long-lived oscillation with a slower decay rate. Let us examine whether the decay rate of quasiparticles characterizing the

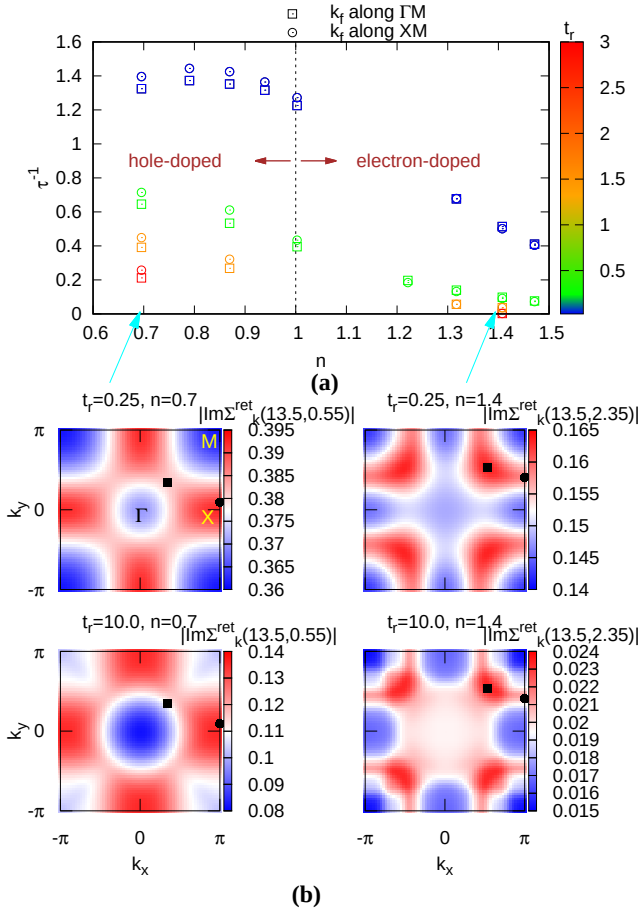

Figure 9. (a) The decay rate, $1/\tau$, of Δn_k against the band filling, at Fermi wavenumbers at $t = 0$ along ΓM (squares) and XM (circles) in the Brilloun zone. The results are obtained for various values of the ramp duration, $t_{\rm r}$ =3.0, 1.5, 0.25, and 0.025 (color-coded). (b) Color plots of the self-energy $|{\rm Im}\Sigma^{\rm ret}_{\boldsymbol{k}}(t,\omega_{\rm qp})|$ at $t = 13.5$, with $\omega_{\rm qp} = 0.55$ for the hole-doped ($n = 0.7$) system (left panels), and at $\omega_{\rm qp} = 2.35$ for the electron-doped ($n = 1.4$) system (right). The results are for $U_{\rm f} = 3$, $\beta = 20$, and $t_{\rm r} = 0.25$ (upper panles) or $t_{\rm r} = 10.0$ (lower). Squares (circles) mark the Fermi momenta at $t = 0$ along ΓM (XM) direction in the Brillouin zone. Note different color codes between different panels.

Green's function describes the inverse relaxation time, τ^{-1}, introduced above. The Fermi-liquid theory predicts that, for a thermal state, the retarded Green's function should have the form[18],

$$G^{\rm ret}_{\boldsymbol{k}}(t) \propto -{\rm Im}\left[e^{-{\rm i}\omega_{\rm qp}t}e^{-\gamma_{\boldsymbol{k}}t}\right], \qquad (23)$$

where $\gamma_{\boldsymbol{k}}$ denotes the relaxation rate. We have checked that this asymptotic form matches fairly well with the retarded Green's function, plotted in middle panels of Fig. 7, for $s > t_{\rm r} + 1/J_1$. Figure 10 (d) displays $\gamma_{\boldsymbol{k}_{\rm f}}$, while Fig. 10 (c) displays $\tau^{-1}_{\boldsymbol{k}_{\rm f}}$, in both of which solid (open) symbols represent the results for Fermi momenta ($\boldsymbol{k}_{\rm f}$) along ΓM (XM) directions in the Brillouin zone. We can see that $\gamma_{\boldsymbol{k}}$ and $\tau^{-1}_{\boldsymbol{k}}$ exhibit similar tendencies against the filling. The slight difference between

Finally to corroborate the thermalization of the doped systems, we present the spin (χ_s), charge (χ_c), and particle-

$\gamma_{\boldsymbol{k}}$ and $\tau^{-1}_{\boldsymbol{k}}$ may be attributed to the remaining non-thermal behavior of the Green's function at $t = 13.5$ as well as to an

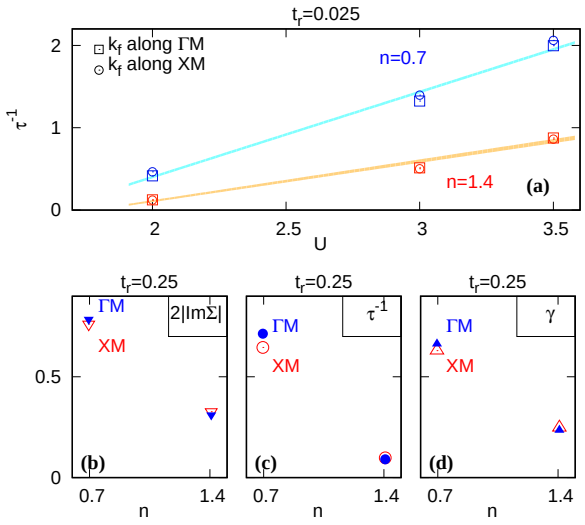

Figure 10. (a) The dependence of the relaxation rate on the Hubbard interaction U at fillings $n = 0.7$ (blue symbols) and $n = 1.4$ (red) along ΓM (squares) and XM (circles) for $t_{\rm r} = 0.025$. Lines are a guide for the eye. The imaginary part of the self-energy ${\rm Im}|\Sigma_{\boldsymbol{k}}|(t,\omega)$ (b), the relaxation rate of $\Delta n_{\boldsymbol{k}}$ (c), and the relaxation rate of the Green's function (d), at $t = 13.5$ and $\omega = \omega_{\rm qp}(\boldsymbol{k})$ against the filling for Fermi momenta along ΓM (solid symbols) and XM (open) for $t_{\rm r} = 0.25$.

error in fitting the short-time data.

In the weak-coupling limit, the Fermi liquid-theory also dictates that, for a thermalized system, the imaginary part of the retarded self-energy at the quasiparticle energy $\omega_{\rm qp}$ corresponds to the inverse quasiparticle lifetime as[45–47]

$$\tau^{-1}_{\rm qp}(\boldsymbol{k}) = -2{\rm Im}\Sigma^{\rm ret}_{\boldsymbol{k}}(t,\omega_{\rm qp}(\boldsymbol{k})), \qquad (24)$$

where the momentum-dependent quasiparticle energy $\omega_{\rm qp}(\boldsymbol{k})$ at time t indicates the position of the peak in $A_{\boldsymbol{k}}(t,\omega)$. To assess whether this relation can also describe the relaxation rate of $\Delta n_{\boldsymbol{k}}$, we compare $2{\rm Im}\Sigma^{\rm ret}_{\boldsymbol{k}}$ and $\tau^{-1}_{\rm qp}(\boldsymbol{k})$ in Fig. 10 (b,c) at Fermi momenta along ΓM and XM directions, associated with $\omega_{\rm qp}(\boldsymbol{k}) = 0.55$ (along ΓM) and 0.65 (along XM) in hole-doped ($n = 0.7$) regime, or $\omega_{\rm qp}(\boldsymbol{k}) = 2.35$ (along ΓM) and 2.45 (along XM) in electron-doped ($n = 1.4$) regime for $t_{\rm r} = 0.25$. Both ${\rm Im}\Sigma$ (b) and $1/\tau$ (c) decrease with the filling. As the self-energy is obtained from the broadened real-time results, a quantitative comparison between the self-energy and the relaxation dynamics is not feasible. Nevertheless, we do notice that ${\rm Im}\Sigma$ and $1/\tau$ deviate more from each other in the hole-doped system. This suggests that the Landau quasiparticle picture may not fully describe the relaxation dynamics in the hole-doped system as the relaxation rate at Fermi surface exceeds the associated $\omega_{\rm qp}$, making the quasiparticle not well-defined.[48,49]

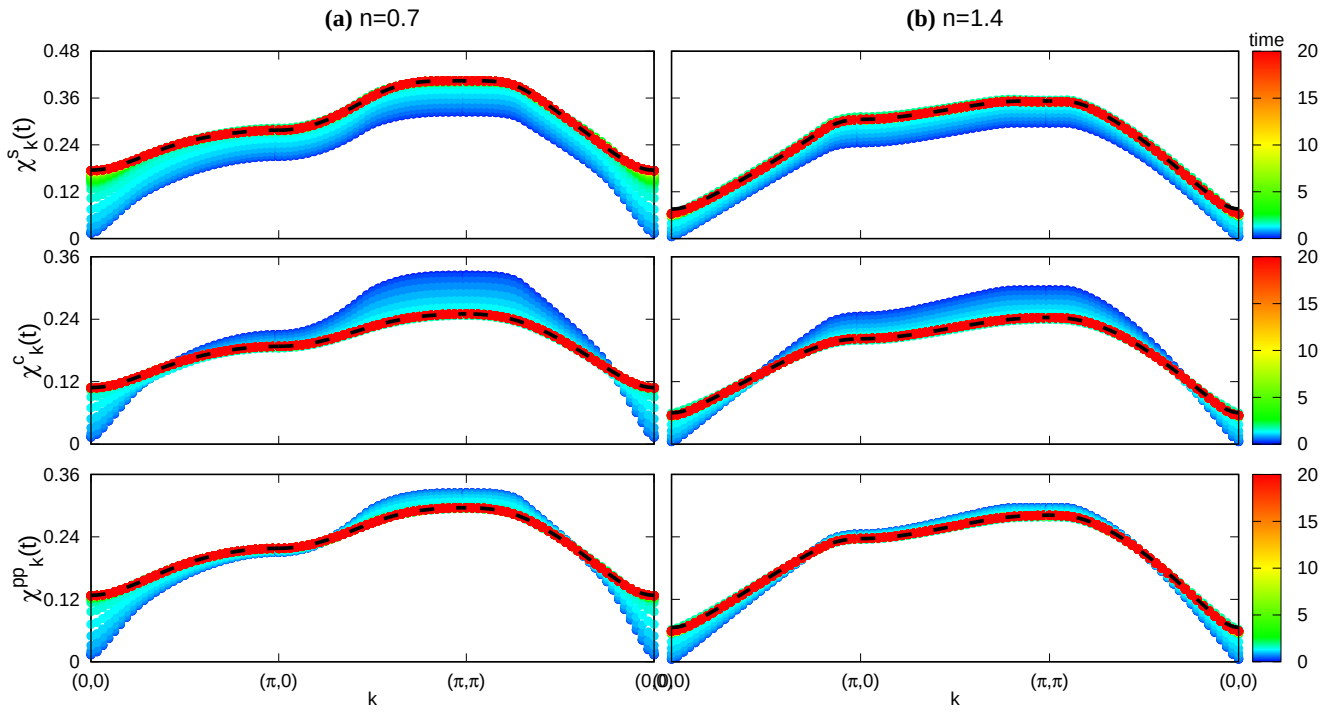

Figure 11. Time evolution (with time color-coded) of the equal-time spin (top panels), charge (middle), and particle-particle (bottom) susceptibilities along high-symmetry lines in the Brillouin zone in hole-doped ($n = 0.7$) (a) and electron-doped ($n = 1.4$) (b) regimes for $U_{\rm f} = 3$, $\beta = 30$ and $t_{\rm r} = 1.5$. Each black dashed line, which almost overlap with the red curve, represent the associated thermal value for each panel.

particle (χ_{pp}) correlation functions in Fig. 11. We find that these two-particle quantities exhibit significant *momentum-dependent evolutions*, which saturates toward a thermal value, see black points in Fig. 11. Also, the result in the hole-doped regime exhibits different relaxation timescales, in particular, between spins and charges, c.f. upper and middle panels in Fig. 11 (a). The effective inverse temperature of the hot electron state upon thermalization for $t_{\rm r} = 1.5$ is $\beta_{\rm eff} = 3.53$ in the hole-doped system ($n = 0.7$), and $\beta_{\rm eff} = 5.13$ in the electron-doped system ($n = 1.4$).

IV. CONCLUSION

We have studied the nonequilibrium dynamics of doped correlated systems under a global ramp of the repulsive Hubbard interaction. From the thermalization of both electron-doped and hole-doped systems in the weak-coupling regime, we have shown that the effective temperature of carriers driven out of equilibrium is smaller for longer ramps and larger fillings. We have discussed that for long ramps the energy density pumped to the system is smaller, hence the system does not occupy highly excited states. For the doping-dependency of the effective temperature, we have explained that in the electron-doped regime the energy cost for hopping of electrons to different sites is greater, which consequently reduces the probability of forming mobile carriers. More importantly, we have identified momentum-dependent relaxations of the distribution function that occurs in a doping-dependent manner.

We have then revealed that, for the hole-doped system, the nonequilibriuim relaxation dynamics is distinct between the "hot- and cold spots" (in the language of equilibrium physics) on the Fermi surface, while the momentum-dependence becomes less pronounced in the electron-doped systems. We have examined how this would fit with the quasiparticle picture in the Fermi-liquid theory. The present results show that, for the hole-doped system, where thermal relaxation governs the dynamics, quasiparticle is not neccessarily well-defined, whereas in the electron-doped system which has lower effective temperature, the Fermi-liquid picture is more well-defined. We have finally presented the temporal evolution of equal-time two-body spin, charge and particle-particle correlation functions. We have shown that for small ramps the system is thermalized, which we have corroborated by comparing the final two-body observables with their thermal counterparts.

Further exploration of the relaxation dynamics of doped systems will require studying the system at lower initial temperatures to allow the ordered phases to appear in thermalization. It is also interesting to investigate this problem in a spin-polarized cases where the spin imbalance will enhance growth of magnetic correlations. Studying multi-band systems with anisotropic coupling parameters is another intriguing problem, which will shed more light on the formation of

spatially modulated orders, which we leave for further studies.

ACKNOWLEDGMENTS

The numerical calculations have been carried out at the ISSP Supercomputer Center at the University of Tokyo. Sh.S. would like to thank N. Kawashima for providing further computational resources. Sh.S. and H.A. acknowledge the support of the ImPACT Program of the Council for Science, Technology and Innovation, Cabinet Office, Government of Japan (GrantNo. 2015-PM12-05-01) from JST. H.A. is also supported by JSPS KAKENHI Grant No. JP26247057. M.C. acknowledge support from the H2020 Framework Programme, under ERC Advanced GA No. 692670 "FIRSTORM", MIUR PRIN 2015 (Prot. 2015C5SEJJ001) and SISSA/CNR project "Superconductivity, Ferroelectricity and Magnetism in bad metals" (Prot. 232/2015).

[1] C. Giannetti, M. Capone, D. Fausti, M. Fabrizio, F. Parmigiani, and D. Mihailovic, Advances in Physics **65**, 58 (2016).
[2] L. Perfetti, P. A. Loukakos, M. Lisowski, U. Bovensiepen, H. Berger, S. Biermann, P. S. Cornaglia, A. Georges, and M. Wolf, Phys. Rev. Lett. **97**, 067402 (2006).
[3] T. Konstantinova, J. D. Rameau, A. H. Reid, O. Abdurazakov, L. Wu, R. Li, X. Shen, G. Gu, Y. Huang, L. Rettig, I. Avigo, M. Ligges, J. K. Freericks, A. F. Kemper, H. A. Dürr, U. Bovensiepen, P. D. Johnson, X. Wang, and Y. Zhu, Science Advances **4** (2018).
[4] C. L. Smallwood, J. P. Hinton, C. Jozwiak, W. Zhang, J. D. Koralek, H. Eisaki, D.-H. Lee, J. Orenstein, and A. Lanzara, Science **336**, 1137 (2012).
[5] C. L. Smallwood, W. Zhang, T. L. Miller, C. Jozwiak, H. Eisaki, D.-H. Lee, and A. Lanzara, Phys. Rev. B **89**, 115126 (2014).
[6] J. Demsar, R. D. Averitt, K. H. Ahn, M. J. Graf, S. A. Trugman, V. V. Kabanov, J. L. Sarrao, and A. J. Taylor, Phys. Rev. Lett. **91**, 027401 (2003).
[7] S. L. Johnson, M. Savoini, P. Beaud, G. Ingold, U. Staub, F. Carbone, L. Castiglioni, M. Hengsberger, and J. Osterwalder, Structural Dynamics **4**, 061506 (2017).
[8] D. H. Torchinsky, J. W. McIver, D. Hsieh, G. F. Chen, J. L. Luo, N. L. Wang, and N. Gedik, Phys. Rev. B **84**, 104518 (2011).
[9] M. K. Chan, C. J. Dorow, L. Mangin-Thro, Y. Tang, Y. Ge, M. J. Veit, G. Yu, X. Zhao, A. D. Christianson, J. T. Park, Y. Sidis, P. Steffens, D. L. Abernathy, P. Bourges, and M. Greven, Nature Communications **7**, 10819 (2015).
[10] G. R. Stewart, Advances in Physics **66**, 75 (2017).
[11] W. Hu, S. Kaiser, D. Nicoletti, C. R. Hunt, I. Gierz, M. C. Hoffmann, M. Le Tacon, T. Loew, B. Keimer, and A. Cavalleri, Nature Materials **13**, 705 (2014).
[12] J. Graf, C. Jozwiak, C. L. Smallwood, H. Eisaki, R. A. Kaindl, D.-H. Lee, and A. Lanzara, Nature Physics **7**, 805 (2011).
[13] Y. Ishida, T. Saitoh, T. Mochiku, T. Nakane, K. Hirata, and S. Shin, Scientific Reports **6**, 18747 (2016).
[14] R. Cortés, L. Rettig, Y. Yoshida, H. Eisaki, M. Wolf, and U. Bovensiepen, Phys. Rev. Lett. **107**, 097002 (2011).
[15] B. Keimer, S. A. Kivelson, M. R. Norman, S. Uchida, and J. Zaanen, Nature **518**, 179 (2015).
[16] N. Tsuji, P. Barmettler, H. Aoki, and P. Werner, Phys. Rev. B **90**, 075117 (2014).
[17] J. Bauer, M. Babadi, and E. Demler, Phys. Rev. B **92**, 024305 (2015).
[18] N. Dasari and M. Eckstein, Phys. Rev. B **98**, 235149 (2018).
[19] K. Ido, T. Ohgoe, and M. Imada, Science Advances **3** (2017), 10.1126/sciadv.1700718.
[20] C. Kollath, A. M. Läuchli, and E. Altman, Phys. Rev. Lett. **98**, 180601 (2007).
[21] J.-M. Bischoff and E. Jeckelmann, Phys. Rev. B **96**, 195111 (2017).
[22] H. Aoki, N. Tsuji, M. Eckstein, M. Kollar, T. Oka, and P. Werner, Rev. Mod. Phys. **86**, 779 (2014).
[23] M. Eckstein, M. Kollar, and P. Werner, Phys. Rev. Lett. **103**, 056403 (2009).
[24] N. Tsuji, M. Eckstein, and P. Werner, Phys. Rev. Lett. **110**, 136404 (2013).
[25] M. Schiró and M. Fabrizio, Phys. Rev. Lett. **105**, 076401 (2010).
[26] N. E. Bickers and S. R. White, Phys. Rev. B **43**, 8044 (1991).
[27] N. E. Bickers, D. J. Scalapino, and S. R. White, Phys. Rev. Lett. **62**, 961 (1989).
[28] K. Kuroki, R. Arita, and H. Aoki, Phys. Rev. B **60**, 9850 (1999).
[29] T. Oka and H. Aoki, Phys. Rev. B **82**, 064516 (2010).
[30] T. Ayral and O. Parcollet, Phys. Rev. B **92**, 115109 (2015).
[31] Y. Yanase and K. Yamada, Journal of the Physical Society of Japan **70**, 1659 (2001).
[32] M. Kitatani, N. Tsuji, and H. Aoki, Phys. Rev. B **92**, 085104 (2015).
[33] H. Sakakibara, H. Usui, K. Kuroki, R. Arita, and H. Aoki, Phys. Rev. Lett. **105**, 057003 (2010).
[34] G.-B. Jo, Y.-R. Lee, J.-H. Choi, C. A. Christensen, T. H. Kim, J. H. Thywissen, D. E. Pritchard, and W. Ketterle, Science **325**, 1521 (2009).
[35] M. Ligges, I. Avigo, D. Golež, H. U. R. Strand, Y. Beyazit, K. Hanff, F. Diekmann, L. Stojchevska, M. Kalläne, P. Zhou, K. Rossnagel, M. Eckstein, P. Werner, and U. Bovensiepen, Phys. Rev. Lett. **120**, 166401 (2018).
[36] L. V. Keldysh, Sov. Phys. JETP **20**, 1018 (1965).
[37] A. Kamenev, *Field Theory of Non-Equilibrium Systems* (Cambridge University Press, 2011).
[38] G. Baym and L. P. Kadanoff, Phys. Rev. **124**, 287 (1961).
[39] K. Aryanpour, M. H. Hettler, and M. Jarrell, Phys. Rev. B **67**, 085101 (2003).
[40] T. Dahm, L. Tewordt, and S. Wermbter, Phys. Rev. B **49**, 748 (1994).
[41] J. Gukelberger, L. Huang, and P. Werner, Phys. Rev. B **91**, 235114 (2015).
[42] J. K. Freericks, H. R. Krishnamurthy, and T. Pruschke, Phys. Rev. Lett. **102**, 136401 (2009).
[43] M. Moeckel and S. Kehrein, New Journal of Physics **12**, 055016 (2010).
[44] M. Eckstein and M. Kollar, New Journal of Physics **12**, 055012 (2010).
[45] C. Hodges, H. Smith, and J. W. Wilkins, Phys. Rev. B **4**, 302 (1971).
[46] P. B. Allen, Phys. Rev. Lett. **59**, 1460 (1987).
[47] M. Sentef, A. F. Kemper, B. Moritz, J. K. Freericks, Z.-X. Shen, and T. P. Devereaux, Phys. Rev. X **3**, 041033 (2013).
[48] C. Berthod, J. Mravlje, X. Deng, R. Žitko, D. van der Marel, and A. Georges, Phys. Rev. B **87**, 115109 (2013).
[49] S. Sayyad and M. Eckstein, Phys. Rev. Lett. **117**, 096403 (2016).